ORIGINAL RESEARCH ARTICLE

Development and Mechanical Characterization of a CoCr-Based Multiple-Principal-Element Alloy

A. Padilla-González[1] · G. González[1,2] · I. Alfonso[3] · A. L. Vidilli[4,5] · L. B. Otani[5] · I. A. Figueroa[1]

Abstract

The development and mechanical characterization of a CoCr-based multiple-principal-element alloy are presented and discussed. In this work, *ab initio* synthesis and mechanical characterization of the $(CoCr)_{100-x}(TiNbZr)_x$ ($x = 0$, 48 60, 78 and 100 % at) alloy family is reported; these include the calculation of thermodynamic parameters such as mixing entropy (ΔS_{mix}), mixing enthalpy (ΔH_{mix}), valence electron concentration (VEC), Ω and δ factors. The alloys were melted in a vacuum arc furnace; rod-shaped ingots were produced by suction casting. Phase characterization was carried out using optical microscopy, scanning electron microscopy (SEM), energy-dispersive X-ray spectroscopy (EDS), and X-ray diffraction. Mechanical characterization was done via compressive and hardness tests. Calculation of phase diagrams was performed using Thermo-Calc © software. Yang's model for phase prediction predicted a BCC solid solution. Multicomponent simulations predicted a more complex structure, with Laves (C14 and C15), Theta (C16), BCC 1, 2 and 3, Mu, $CoTi_2$, $CoZr_3$ and $TiZr_2$. Contrary to Yang's model for phase prediction, the experimentally obtained phases agreed reasonability well with those obtained by the Thermo-Calc simulation. The suction cast process cooling rate suppressed the nucleation and growth of some equilibrium phases, i.e., Laves (C14) or BCC 3 for the $(CoCr)_{100-x}(TiNbZr)_x$ ($x = 0$, 48 60, 78 and 100 % at) alloys. The hardness test results were strongly related to the intermetallic phase formation, showing an increase of 331% with the $x = 78$ alloy. The BCC 1 phase played an important role in the yield strength behavior, as the $(CoCr)_{22}(TiNbZr)_{78}$ alloy, with a considerable amount of this phase, showed the highest yield strength value.

Keywords Cobalt alloys · Intermetallics · Microstructure · Titanium alloys

✉ G. González
joseggr@unam.mx

✉ I. A. Figueroa
iafigueroa@unam.mx

1 Instituto de Investigaciones en Materiales, Universidad Nacional Autónoma de México, Circuito Exterior S/N, Cd. Universitaria, C.P. 04510 México City, México

2 Instituto de Tecnología de Materiales, Universitat Politècnica de València, Camino de Vera s/n, 46022 Valencia, Spain

3 Instituto de Investigaciones en Materiales, Unidad Morelia, Universidad Nacional Autónoma de México, Campus Morelia, Antigua Carretera a Pátzcuaro No. 8701, Col. Ex-Hacienda de San José de la Huerta, CP. 58190 Morelia, Michoacán, México

4 Graduate Program in Materials Science and Engineering, Universidade Federal de São Carlos, Rod. Washington Luis, s/n-Monjolinho, São Carlos, SP 13565–905, Brazil

5 Department of Materials Engineering (DEMa), Universidade Federal de São Carlos, Rod. Washington Luis, km 235, São Carlos, SP 13565–905, Brazil

Introduction

Multiple-principal-element (MPE) alloys are novel materials. They were first described by Ranganathan in 2003, then by Jien-Wei Yeh and Brian Cantor in 2004. The definitions of these materials are broad. Nevertheless, MPE alloys are metallic materials composed of 5 or more elements in equal or quasi-equal proportions. These materials propose a new approach to design and an interesting combination of properties that could lead to specifically designed parts or devices [1–4].

The TiNbZr alloy presents a good combination of mechanical properties. Its elastic behavior has been mainly studied and could be potentially used in the aerospace or medical industries or even as a structural material; nevertheless, as far as we are aware, it has not been used in any practical application due to its poor wear resistance [5–8].

On the other hand, CoCr alloys have been used in dental implants or orthopedic devices. These alloys have a high

resistance but are too hard and brittle, making them difficult to machine. MPE alloy could combine these properties and give these alloys a more practical use as structural materials or in medical devices [9–11].

In order to design MPE alloys, Zhang et al. have proposed a predictive model for phase formation using Boltzmann's thermodynamic statistics equations for mixing entropy (ΔS_{mix}) and mixing enthalpy (ΔH_{mix}). This model provides a way of correlating the obtained values proposing other parameters called "Ω" and the atomic size difference "δ" [4, 12, 13].

In this model, $\Delta \mathbf{S}_{\mathrm{mix}}$ can be calculated as [4, 12]:

$$\Delta S_{\mathrm{mix}} = -R \sum_{i=1}^{n} (c_i \ln c_i) \tag{1}$$

where R represents the gas constant, and c_i is the molar fraction of component i.

Using similar approximations, $\Delta \mathrm{H}_{\mathrm{mix}}$ can be calculated by the following equation [4, 12]:

$$\Delta H_{\mathrm{mix}} = \sum_{i=1,i\neq j}^{n} 4\Delta H_{\mathrm{mix}(i,j)} c_i c_j \tag{2}$$

where $\Delta H_{\mathrm{mix}(i,j)}$ is the mixing enthalpy for the binary equiatomic i–j alloys. It is worth mentioning that there are several ways of calculating the $\Delta H_{\mathrm{mix}(i,j)}$; however, in this work, the Miedema's model was used. The Miedema's model values can be calculated using Eq 3 [14–16]:

$$\Delta H_{\mathrm{mix}(i,j)} = \frac{c_i V_{\mathrm{Aalloy}}^{\frac{2}{3}}}{\left[(n_{\mathrm{ws}}^{i})^{-\frac{1}{3}} + (n_{\mathrm{ws}}^{j})^{--\frac{1}{3}} \right]} \left[-P(\Delta \Phi^*)^2 + Q\left(\Delta n_{\mathrm{ws}}^{\frac{1}{3}} \right)^2 - R_m \right] f_j^i \tag{3}$$

These values can be obtained by substituting Eqs 4–7 in 3.

$$f_j^i = c_j^s \left[1 + 8\left(c_i^s c_j^s \right)^2 \right] \tag{4}$$

$$c_i^s = \frac{c_i V_i^{\frac{2}{3}}}{c_i V_i^{\frac{2}{3}} + (1-c_i) V_j^{\frac{2}{3}}} \tag{5}$$

$$c_j^s = 1 - c_i^s \tag{6}$$

$$V_{\mathrm{alloy}}^{\frac{2}{3}} = V_i^{\frac{2}{3}} * [1 + a.cf * f_j^i\left(\phi_i^* - \phi_j^* \right)] \tag{7}$$

where n_{ws} are the electron density at the Wigner–Seitz cell boundary. φ_i and φ_j represent the electronegativity of elements i and j. A table of these values for some transition metals can be obtained in Miedema et al. original work [16].

V_i and V_j are the molar volume of the i and j element. P, Q, $\mathbf{R}_m$, α and a.c f are constants determined by Miedema et al.

Reference [14] provides a more accurate description of all the parameters employed in this model.

On the other hand, δ is defined by the following equation [4, 12, 17]:

$$\delta = \sqrt{\sum_{i=1}^{n} c_i \left(1 - \frac{r_i}{\bar{r}} \right)^2} \tag{8}$$

where r_i and $\underline{r}$ represent the atomic radius for the ith element and the average radii of the elements that constitute the alloy ($\bar{r} = \sum_{i=1}^{n} c_i r_i$), respectively.

The last parameter employed as a predictive model for MPE alloys is Ω; this parameter is defined as:

$$\Omega = \frac{T_M \Delta S_{\mathrm{mix}}}{\Delta H_{\mathrm{mix}}} \tag{9}$$

where T_M represents the average fusion temperature of the alloy ($T_M = \sum_{i=1}^{n} c_i T_{Mi}$) and can be estimated from the melting temperature of each element. In this equation, T_{Mi} represents the melting temperature of the ith element. In general, it has been proposed that the formation of a stable solid solution in an MPE alloy occurs when $12 \leq \Delta S_{\mathrm{mix}} \leq 17.5$ J/molK, $-20 \leq \Delta H_{\mathrm{mix}} \leq 5$ kJ/mol, $\Omega \geq 1.1$ and $\delta \leq 6.6\%$ [4, 12, 13, 18, 19].

Once MPE alloys were described, many of them were developed; it has been noted that most of these alloys have a body-centered cubic (BCC) or face-centered cubic (FCC) structure. To predict which of these structures will be adopted by a particular alloy, the valence electron concentration (VEC) model is widely used. Mathematically, VEC is defined as [4, 20, 21]:

$$\mathrm{VEC} = \sum_{i=1}^{n} c_i \mathrm{VEC}_i \tag{10}$$

It has been noted that when VEC < 6.87, the structure adopted by the alloy will be BCC; when 6.87 < VEC < 8.0, a mixture of BCC and FCC structures will be obtained. Finally, when VEC > 8.0, a pure FCC will be formed [4, 21].

From the above, the objective of this work was to generate the high-entropy alloys described by the general formulae (CoCr)100-x(TiNbZr)x ($x = 0$, 48, 60, 78 and 100 % at) and study their mechanical properties. The aim was to obtain an alloy that outclassed the mechanical properties of TiNbZr alloy, such as the elastic modulus, yield

strength and ultimate compressive strength, while keeping its plastic properties.

Experimental Procedure

Calculations of ΔS_{mix} and ΔH_{mix} were made using Boltzmann's and Miedema's models for alloys containing Co, Cr, Ti, Nb and Zr. This process was carried out to predict the formation of a homogenous solid solution of the selected elements, while Tm was calculated based on the rule of mixture. Finally, Ω and δ factors were also calculated from Zhang et al. proposed model [13]. From the above, the calculated chemical compositions for casting the alloy samples were $(CoCr)_{100-x}(TiNbZr)_x$ ($x=0$, 48 60, 78 and 100 % at). Co, Cr, Ti, Zr, and Nb pellets with purity higher than 99.5% were used as starting materials for the alloy samples. The ingots (10 g) were melted five times in a vacuum arc furnace to ensure a homogenous composition. After solidification, the obtained ingots were melted and suction cast into cylindrical rods that complied with ASTM-E9-19 standards. Without any heat treatment, as-cast samples were employed to keep the rapidly cooled microstructure obtained through the suction casting process. Phase characterization was made on transversal cut samples of the suction cast rods. Samples were grounded using sandpaper with increasingly small particle sizes and polished with alumina down to 0.04 μm. The chemical composition of ingots was obtained by energy-dispersive X-ray spectroscopy (EDS), and images were obtained with a JEOL-7600 Schottky field emission scanning electron microscope (SEM). XRD patterns were generated using a Bruker D8 Advanced with Cu kα radiation. Compressive tests were performed on rods of 6 mm in diameter by 5 mm in length, following ASTM-E9-19 standard, using an INSTRON 5500-R universal machine at a strain rate of $4x10^{-4}$ s^{-1}, and microhardness tests measurements were done on a Shimadzu HMV-G machine 100 g with a dwell time of 15 s. It is worth noting that ten indentations were taken for statistical purposes. Finally, the phase equilibria simulation calculations were performed using the Thermo-Calc (2022a) THCEA-3 database (Thermo-Calc Software, Stockholm, Sweden) to compare the experimentally obtained phases with the multicomponent simulations.

Results and Discussion

Thermodynamic Parameters

In order to calculate ΔH_{mix} for each alloy, $\Delta H_{mix\,(I,\,j)}$ must be calculated. Results for these calculations can be found in Fig. 1. It is important to note that negative values represent an exothermic process, while positive ones are endothermic. As the value grows, it indicates how much energy must be spent or liberated in this process, bearing in mind that

the most exothermal mixing process corresponds to mixing cobalt and zirconium, with a value of -39.61 kJ/mol. This means that these two elements have a high affinity for one another. On the other hand, the most endothermal process is mixing niobium and zirconium, with a value of 3.95 kj/mol, forming a solid solution.

The results of the obtained calculations are presented in Table 1. This table shows that for the first alloy, when $x=0$, the values for ΔS_{mix}, ΔH_{mix}, and δ are lower than those obtained at $x=48$, 60 and 78. This is congruent with binary alloys, which have low ΔH_{mix} and similar atomic radii. Nevertheless, the obtained value for Ω at $x=0$ was lower than those obtained at $x=48$, 60 and 78. This is due to the difference between the ΔS_{mix} and ΔH_{mix} values and could be related to the smaller energy required to mix these two elements. A similar analysis can be performed for the $x=100$ alloy; in this case, this alloy classifies as a medium-entropy alloy [4]. For the compositions where $x=48$, 60 and 78, it can be noted that the values for ΔS_{mix}, Ω and δ are very similar; these results suggest that the produced alloys will form solid solutions. It is worth noting that ΔH_{mix} values are far from 0; nevertheless, they are still in the range of forming simple solid solutions. Additionally, an already observed tendency [17] in ΔS_{mix} can be noted; this value reaches its maximum value when the concentrations of all atoms are equal. Finally, VEC results predict a BCC and FCC mixture for the CoCr ($x=0$) alloy and a BCC structure for the other alloys.
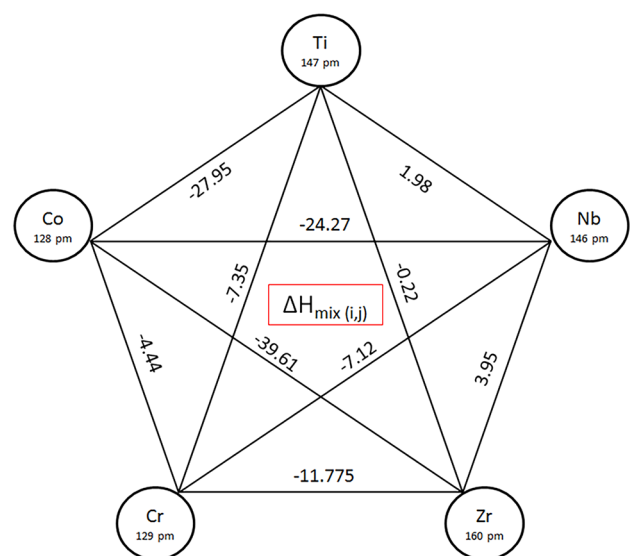

Fig. 1 Results of $\Delta H_{mix\,(I,j)}$. All results are in kj/mol

Table 1 Results of thermodynamic parameters for the $(CoCr)_{100-x}(TiNbZr)_x$ family alloys

X, at.%	Composition	ΔS_{mix}, J/mol*K	ΔH_{mix}, kJ/mol	T_m, K	Ω	δ, %	VEC
0	CoCr	5.76	− 4.44	2017.8	1.32	1.82	7.50
48	$(CoCr)_{52}(TiNbZr)_{48}$	13.14	− 20.01	2059.1	1.35	4.62	5.98
60	$(CoCr)_{40}(TiNbZr)_{60}$	13.38	− 18.69	2086.6	1.49	4.74	5.60
78	$(CoCr)_{22}(TiNbZr)_{78}$	12.77	− 12.80	2127.9	2.12	4.70	5.03
100	TiNbZr	9.13	− 0.76	2155.4	3.96	4.26	4.33

Phase Characterization

Figure 2 A to E shows the SEM images for the suction cast alloys. Figure 2 A corresponds to the CoCr alloy ($x = 0$ at.%); Figure 2B–D corresponds to the alloys with $x = 48$, 60 and 78 at.%, respectively; finally, Fig. 2E corresponds to the TiNbZr alloy. Initially, it can be noted that in the first alloy ($x = 0$), the microstructure comprises two phases, σ and εCo (Fig. 2A). These results are congruent with those previously reported [22–24]. Similarly, for the TiNbZr ($x = 100$) alloy (Fig. 2E), a single solid solution phase was observed, being also previously reported [5, 8, 25].

For the second alloy, when $x = 48$ (Fig. 2B), the addition of TiNbZr to the CoCr matrix caused the formation of three zones with similar mean nucleic mass. First, a precipitate that appears as a light gray area in SEM images, a second formation appears as a darker gray phase, and finally, a black dot phase. In general terms, the morphology obtained was dendritic, despite the fact that thermodynamical calculations (Boltzmann's, Miedema's and Zhang's models) initially predicted the formation of a single solid solution, this was related to the high mixing enthalpy of some of the elemental couples, particularly Co-Cr and Co-Zr (Fig. 1). As this value increases in magnitude, it can indicate the formation of intermetallic phases. A slow cooling rate favors the formation of additional phases, as will be discussed further ahead. Hence, the precipitation of phases indicates that higher cooling rates may be required to form a solid solution. Phase identification was possible via EDS elemental analysis and X-ray diffraction; these results will be discussed below.

The third alloy ($x = 60$) presented a more complex morphology. Only three zones were observed in the SEM image; they can be seen in different gray scales (Fig. 2C). This concentration of TiNbZr prevented the formation of the dendrites observed at the previous amount ($X = 48$); nevertheless, the absence of complete dendrites suggests that this sample had a better response to the selected cooling rate. The equiatomic structure predicted by thermodynamic factors was that of a single solid solution; nevertheless, it appears that the energy needed to mix the individual
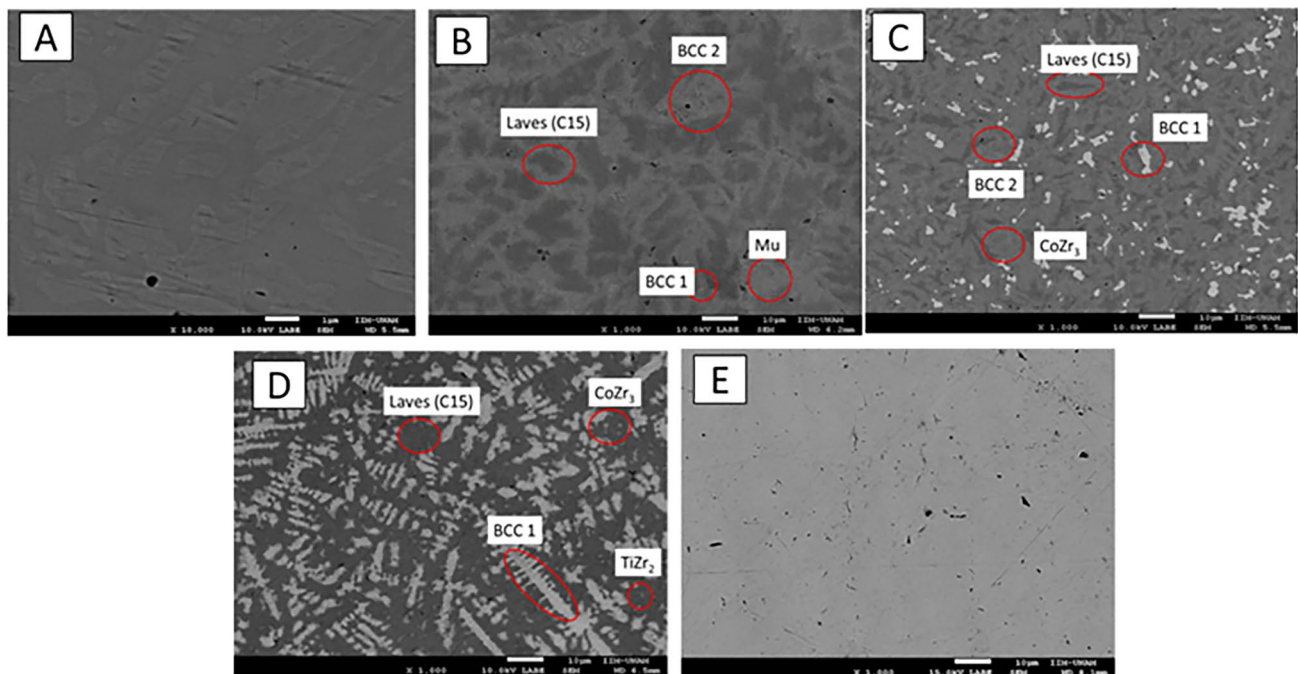

Fig. 2 SEM images for synthetized for the $(CoCr)_{100-x}(TiNbZr)_x$ alloys. (**A–E**) corresponds to the $x = 0$, 48, 60, 78 and 100 %, respectively

elements (ΔH_{mix}) is too high to compensate the entropic factors (ΔS_{mix}), causing the formation of different and more stable structures.

Finally, for the alloy with $x = 78$, the SEM analysis showed a dendritic structure, being observed in two gray scales (Fig. 2D). This alloy showed the biggest dendrites of them all; it is believed this could be an indicator of phase stability, and a possible candidate to form a single solid solution provided a faster cooling rate is applied, as this alloy had the highest Ω factor of the 5 element alloys, which has been previously reported as a favoring condition to form solid solutions [4].

In Figure 3, the results of EDS analysis are shown. Figure 3A–C corresponds to the alloys where $X = 48$, 60 and 78 at.%, respectively. The addition of TiNbZr ($x = 48$) (Fig. 3A) shows a clear, distinct zone (Fig. 2B) containing mainly Zr and Nb. It can also be noted that Co and Nb were more evenly distributed within the sample, being related to the cooling rate. The equiatomic composition yielded in forming Nb and Cr-rich zones (Fig. 3B), even though the higher values of mixing enthalpy with Co could have suggested that these elements would form other phases. All elements could be found in some proportion in each of the observed phases.

Finally, the $(CoCr)_{22}(TiNbZr)_{78}$ alloy produced Nb-rich dendrites with Zr, Ti and Cr (Fig. 3C). Ti could be found in both zones. This composition was expected to produce a solid solution; however, dendrite shape morphologies were observed. Based on this result and the calculated values of Ω and δ, it is suggested that a single solid solution could be produced just by increasing the cooling rate for this particular composition. The EDS-obtained compositions for the observed phases are shown in Table 2. These observed phases could not be identified solely by this technique and were characterized when the analysis was complemented with XRD.

Figure 4A–C presents the diffraction patterns obtained for the alloys where $x = 48$, 60 and 78 at.%. For the $X = 48$ alloy, four phases were detected (Fig. 4A). Two BCC solid solution phases were observed. The third and fourth phases consisted of the intermetallic Laves and Mu phases. This result is promising for the formation of solid solutions, as the formation of two BCC phases indicates that alloy elements are thermodynamically compatible (Fig. 1) to produce a solid solution. This could be achieved if the fabrication parameters, i.e., cooling rate, are modified.

The equiatomic alloy showed four phases (Fig. 4B): a BCC 1 structure composed of Nb, Ti and Zr, a BCC 2 solid solution phase composed of Ti, Nb, Zr and Co, an FCC intermetallic phase with Cr and Zr (Fig. 3B) and finally, as mentioned below when analyzed by XRD, a fourth phase was detected. This phase corresponded to a phase with the characteristics of the intermetallic Laves (C15). Similar to the abovementioned composition, the formation of only

cubic phases is a promising result, as it can be an indicator that these chemical elements could lead to the formation of a single solid solution.

Finally, the alloy where $X = 78$ presented a BCC solid solution with Nb, Zr, Co and Ti, an intermetallic phase composed of Ti_2Co, and a C15 Laves phase. Furthermore, a more detailed analysis with XRD showed the presence of two additional phases primarily composed of Zr with Co and Ti in intermetallic forms (Fig. 4C). These additional phases could be in small concentrations or have a similar atomic weight to the BCC phases, thus making them difficult to observe by SEM or EDS. In Table 3, the lattice parameters for the indexed phases are shown. It is worth mentioning that the phases calculated lattice parameters are rather similar to those reported in the literature [26–30]; however, the small differences between the lattice parameter reported here and those reported could be attributed to the additional atoms in the cell.

As the amount of CoCr increases, the BCC 1 lattice parameter decreases. This solid solution was found in all produced alloys. Therefore, this result could imply that the possibility of nucleating and growing a BCC1 phase is very likely when using these elements. On the other hand, as the CoCr ratio increases, the lattice parameter of the C15 Laves phases shows a slight increase (Table 3). The decrease in the lattice parameter of the C15 Lave phases was attributed to the compositional change in both phase and alloys investigated; this will be theoretically analyzed in the following section (Fig. 5).

The lattice parameters of Mu, $CoZr_3$, Ti_2Co and $TiZr_2$ phases agree reasonably well with those found in the literature. These intermetallic compounds have a stoichiometric fixed composition related to their mixing enthalpy of the pair, making them highly stable. It is interesting to note that despite ΔS_{mix}, VEC, Ω and δ factors predicted the formation of a solid solution, a mixture of phases was obtained, as predicted by ΔH_{mix}. This means that the formation of a solid solution in these alloys is strongly driven by mixing enthalpy. Thus, a heat treatment or higher cooling rate from the melt could be necessary to form a single phase. This hypothesis is based on the fact that the cooling rate of the suction cast rods is much higher than that of the equilibrium condition.

Phase Diagrams

Figure 5 contains the calculated phase diagrams for the produced alloys. In these diagrams, it can be noted that a series of intermetallic phases can be formed. First are the Laves phases, an intermetallic phase with two arrangements, cubic (C15) or hexagonal (C14). Secondly, the Mu phase is a Frank–Kasper-type intermetallic phase composed of Co and Nb with an HCP structure. The formation
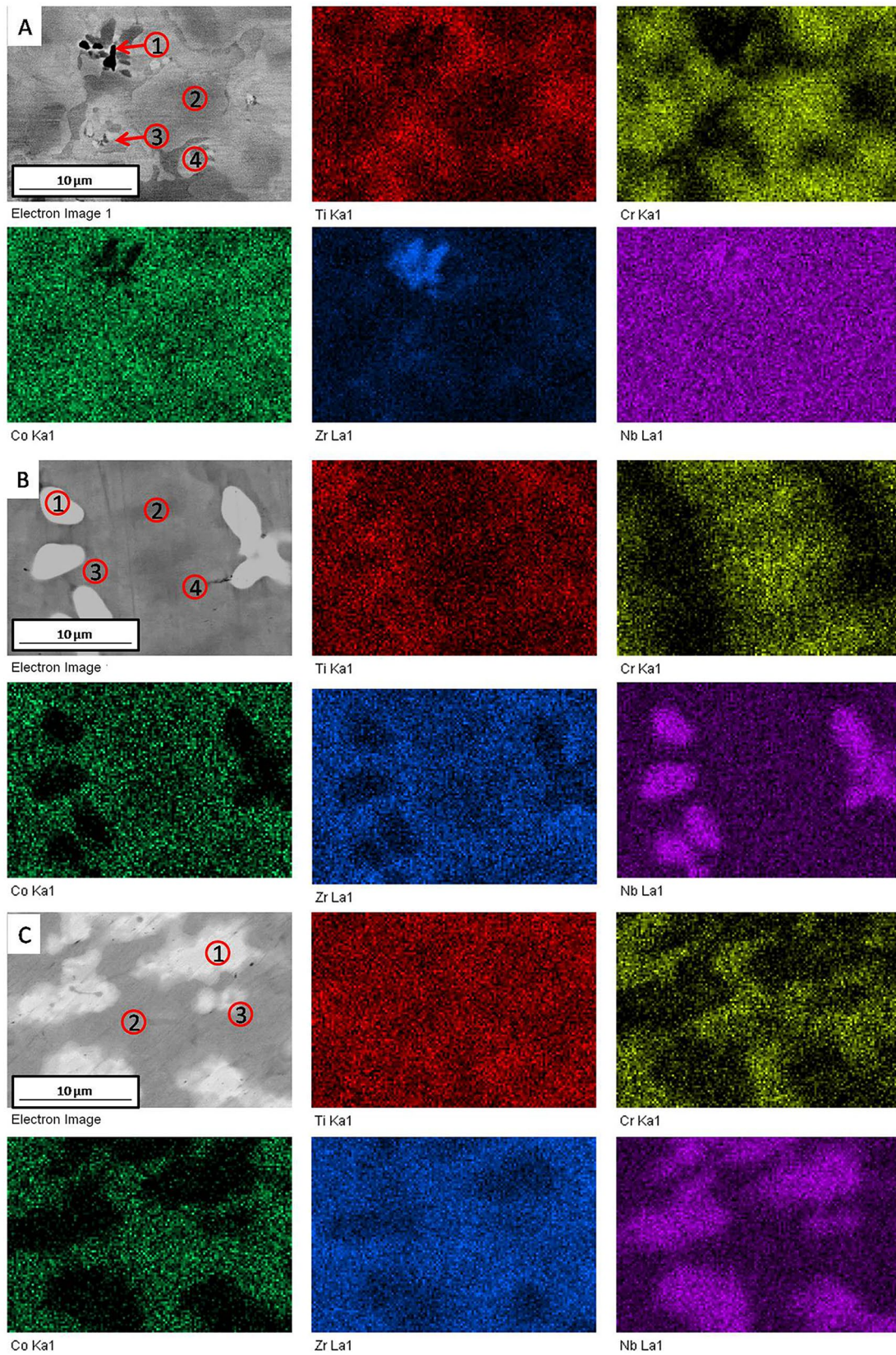
Fig. 3 EDS results for the investigated alloys: (**A**) $(CoCr)_{52}(TiNbZr)_{48}$ alloy. (**B**) $(CoCr)_{40}(TiNbZr)_{60}$ and (**C**) $(CoCr)_{22}(TiNbZr)_{78}$

Table 2 Energy-dispersive X-ray spectroscopy

Composition	Label	Phase	Composition, Atomic %
$(CoCr)_{52}(TiNbZr)_{48}$	1	Laves (C15)	$Co_9Cr_{28}Ti_1Nb_{11}Zr_{51}$
	2	BCC 1	$Co_{49}Ti_{31}Nb_8Zr_{12}$
	3	Mu	$Co_{38}Cr_8Ti_4Nb_{50}$
	4	BCC 2	$Cr_4Ti_{12}Nb_{83}Zr_1$
$(CoCr)_{40}(TiNbZr)_{60}$	1	BCC 1	$Cr_1Ti_{25}Nb_{66}Zr_8$
	2	BCC 2	$Co_{42}Ti_{27}Nb_8Zr_{23}$
	3	$CoZr_3$	$Co_{26}Zr_{74}$
	4	Laves (C15)	$Co_4Cr_{60}Ti_2Nb_2Zr_{31}$
$(CoCr)_{22}(TiNbZr)_{78}$	1	BCC 1	$Cr_{10}Ti_{25}Nb_{52}Zr_{13}$
	2	Laves (C15)	$Co_5Cr_{61}Ti_2Zr_{32}$
	3	$TiZr_2 + CoZr_3$	$Co_9Ti_{10}Nb_2Zr_{69}$
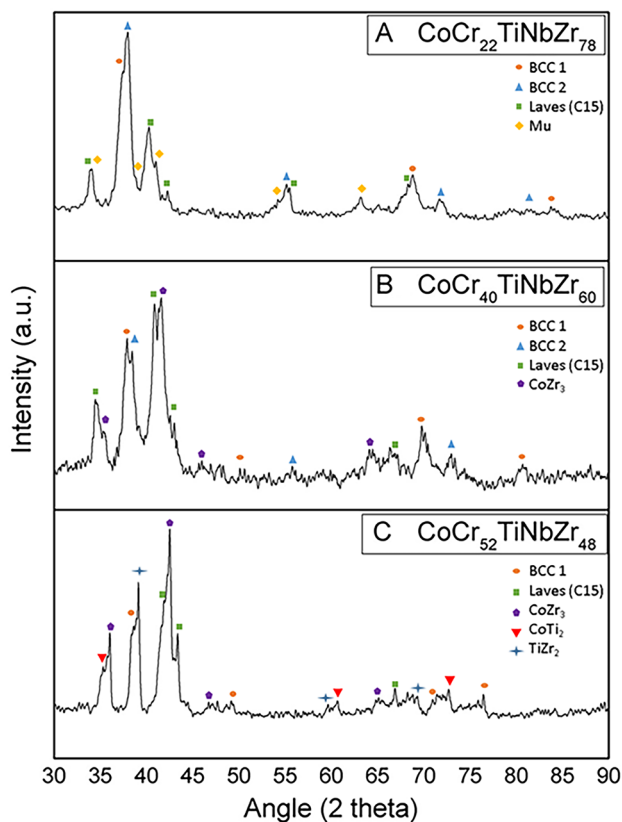
Fig. 4 X-ray diffraction pattern for (**A**) $(CoCr)_{22}(TiNbZr)_{78}$. (**B**) $(CoCr)_{40}(TiNbZr)_{60}$ and C) $(CoCr)_{52}(TiNbZr)_{48}$ alloy

of other binary intermetallic phases was also predicted, i.e., $CoTi_2$, $CoZr_3$ and $TiZr_2$. Finally, three BCC solid solution phases were also predicted.

Figure 5 A shows that the $(CoCr)_{52}(TiNbZr)_{48}$ alloy has six possible phases. At room temperature and in equilibrium conditions, this alloy presents four phases, i.e., BCC 1 and 2, a C15 Laves phase and Mu. Despite

the cooling rate employed, all these phases were also observed through XRD (Fig. 4 A). This phenomenon can be attributed to the high mixing enthalpy of the involved elements, which causes the formation of precipitates despite the fast-cooling rate. Since a higher amount of BCC than the Mu phase was found, phase transformations were believed to be stopped between 350 and 250 °C.

Simulations for $(CoCr)_{40}(TiNbZr)_{60}$ can be found in Fig. 5B. These simulations showed that there are seven possible phases. In equilibrium conditions and at 20 °C, the system should have five phases: BCC 1 and 2, a C15 Laves and two intermetallic phases, i.e., $CoZr_3$ and $CoTi_2$. Similar to the previous alloy, the intermetallic phases are highly expected due to their high ΔH_{mix} (Fig. 1). Nevertheless, only $CoZr_3$ and (C15) Laves were found in the suction cast samples. In equilibrium conditions, the $CoTi_2$ phase should occupy nearly 20% of the sample; however, it was not found in the XRD patterns. It is believed that the absence of this phase is related to the increased solubility of Co and Zr in the Laves phase at high temperatures; then, when the sample is cast and rapidly cooled, the nucleation process is avoided. The hypothesis that the Laves phase is responsible for the absence of a Co-Zr precipitate is supported by the observation that the composition of the BCC phases remains with little to no change in composition as temperature changes (Fig. 5, insert); thus, the increase in solubility of Co and Zr in the Laves phase occurred.

Finally, results for the alloy when $x = 78$ at.% are also presented (Fig. 5C). This sample should have four phases in equilibrium conditions and at room temperature: the C15 Laves phase, the intermetallics $TiZr_2$ and $CoTi_2$, and the BCC 1 solid solution. However, five phases were detected in the XRD patterns (Fig. 4C). It is believed that the presence of the $CoZr_3$ intermetallic compound in the microstructure is related to the high cooling rate, stopping the phase transformations at ~150 °C and producing a nonequilibrium phase at room temperature. The absence of BCC 3 within the final microstructure supports the abovementioned hypothesis, i.e., the arrest of the microstructure that could have been produced between 150 and 450 °C. This frozen microstructure was definitely produced during the high cooling rate casting.

Mechanical Characterization

Hardness Tests

Figure 6 presents the mean obtained results and their standard deviation from the hardness test. In this figure, it can be noted that as the amount of CoCr increases, the hardness of the alloy also increases. This could be attributed to the

Table 3 Calculated and reported lattice parameters for the found phases in the family of alloys $(CoCr)_{100-x}(TiNbZr)_x$ with ($x = 0$, 48 60, 78 and 100 at.%)

$(CoCr)_{52}(TiNbZr)_{48}$		$(CoCr)_{40}(TiNbZr)_{60}$		$(CoCr)_{22}(TiNbZr)_{78}$		
Phase	Measured Lattice parameter, Å	Phase	Measured Lattice parameter, Å	Phase	Measured Lattice parameter, Å	Reported lattice parameter, Å
C15 Laves	a 7.2257	C15 Laves	a 7.0618	C 15 Laves	a 7.0619	a 7.0210 [26]
BCC 1	a 3.3062	BCC 1	a 3.3620	BCC 1	a 3.3698	Not available
BCC 2	a 3.2538	BCC 2	a 3.3125			Not available
Mu ($Co_{46}Nb_{54}$)	a 4.9970 c 26.1604 hexagonal					a 4.9040 c 26.1860 [27]
		$CoZr_3$	a 3.2746 b 10.4466 c 8.9345	$CoZr_3$	a 3.2679 b 10.4747 c 8.9461	a 3.277 b 10.904 c 8.99 [28]
				Ti_2Co ($Ti_{67}Co_{33}$)	a 11.2900	a 11.2881 [29]
				$TiZr_2$ ($Ti_{36}Zr_{64}$)	a 3.1502 b 5.0451	a 3.148 b 5.054 [30]

formation of intermetallic phases into the original solid solution microstructure. The obtained values range from 264 HV for $x = 0$ to a maximum of 876 HV for $x = 78$, representing an increment of 331% in hardness. The obtained hardness values suggest that intermediate concentrations of CoCr in the alloy matrix, i.e., between 40 and 60%, produced alloys with the highest hardness value. For the alloy without CoCr, a softer BCC solid solution microstructure was obtained; however, harder Laves and Mu phases were formed for the alloy with 52 at.% of CoCr, which generated the increase mentioned above in hardness. This hardness could be comparable to hot work tool steels (480–740 HV) [33]

Compression Tests

In Figure 6, the results of the compression tests are shown. From this figure, the high mechanical properties of both TiNbZr and CoCr can be noted. For the CoCr, the yield strength was 1300 MPa, showing brittle behavior and fracturing before any plastic deformation occurred. Regarding the TiNbZr alloy, the yield strength was 784 MPa, but the plastic deformation behavior was considerably higher. It can be noted that there was a significant decrease in yield strength for two of the tested compositions, i.e., $(CoCr)_{52}(TiNbZr)_{48}$ and $(CoCr)_{40}(TiNbZr)_{60}$, reached 84.4 and 107.7 MPa, respectively. It is believed that this decrement in mechanical properties could be related to the BCC1 phase; as the amount of this phase increases, so does the

yield strength. This can be supported by the results presented in Fig. 2 (white zones), 3 (XRD peaks) and 5 (CALPHAD), where the BCC1 phase grew as the amount of TiNbZr increased. Finally, it is thought that the brittle behavior could be attributed to the nucleation and growth of the intermetallic phases in the alloys with CoCr additions since the TiNbZr alloy just showed the ductile BCC1 phase (Fig. 7).

Conclusions

The family of MPE alloys described by $(CoCr)_{100-x}(TiNbZr)_x$ with $x = 0$, 48 60, 78 and 100 at.% were produced. The initial thermodynamical calculations based on Boltzmann's and Miedema's models predicted that these alloys would be constituted primarily by a BCC solid solution. On the other hand, the multicomponent simulations predicted a more complex structure, with Laves (C14 and C15), Theta (C16), BCC 1, 2 and 3, Mu, $CoTi_2$, $CoZr_3$ and $TiZr_2$. The experimentally obtained phases agreed reasonability well with those obtained by the Thermo-Calc simulation, contrary to that of the Boltzmann's and Miedema's models, where the magnitude of ΔS_{mix}, VEC, Ω and δ factors predicted the formation of a solid solution; nevertheless, a mixture of phases was obtained, as predicted by ΔH_{mix}. It is though those small differences observed by SEM and XRD but reported by THERMO-CALC, it could be explained in terms of the resulting cooling rate of the suction casting process. From

A (CoCr)$_{52}$(TiNbZr)$_{48}$
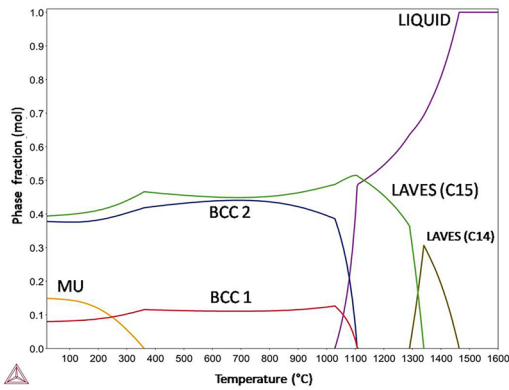
TEMPERATURE	PHASE	COMPOSITION	TEMPERATURE	PHASE	COMPOSITION
1400°C	LIQUID	Co$_{28}$Cr$_{21}$Ti$_{18}$Nb$_{15}$Zr$_{18}$	700°C	LAVES (C15)	Co$_9$Cr$_{58}$Ti$_1$Nb$_{11}$Zr$_{21}$
	LAVES (14)	Co$_{19}$Cr$_{47}$Ti$_7$Nb$_{20}$Zr$_7$		BCC 1	Co$_{50}$Ti$_{35}$Zr$_{15}$
				BCC 2	Cr$_1$Ti$_2$Nb$_{97}$
1300°C	LIQUID	Co$_{29}$Cr$_{15}$Ti$_{21}$Nb$_{16}$Zr$_{19}$	300°C	LAVES (C15)	Co$_8$Cr$_{59}$Nb$_6$Zr$_{27}$
	LAVES (C14)	Co$_{20}$Cr$_{45}$Ti$_8$Nb$_{21}$Zr$_7$		BCC 1	Co$_{50}$Ti$_{40}$Zr$_{10}$
	LAVES (C15)	Co$_{20}$Cr$_{47}$Ti$_6$Nb$_{15}$Zr$_{12}$		BCC 2	Nb
				Mu	Co$_{46}$Nb$_{54}$
1000°C	LAVES (C15)	Co$_{14}$Cr$_{53}$Ti$_4$Nb$_{11}$Zr$_{18}$	20°C	LAVES (C15)	Cr$_{66}$Zr$_{34}$
	BCC 1	Co$_{49}$Ti$_{31}$Nb$_1$Zr$_{19}$		BCC 1	Co$_{50}$Ti$_{42}$Zr$_8$
	BCC 2	Cr$_4$Ti$_{12}$Nb$_{83}$Zr$_1$		BCC 2	Nb
				Mu	Co$_{46}$Nb$_{54}$

B (CoCr)$_{40}$(TiNbZr)$_{60}$
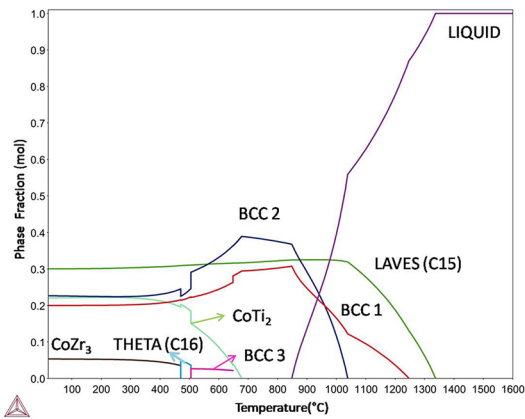
TEMPERATURE	PHASE	COMPOSITION	TEMPERATURE	PHASE	COMPOSITION
1300°C	LIQUID	Co$_{21}$Cr$_{17}$Ti$_{21}$Nb$_{20}$Zr$_{21}$	300°C	LAVES (C15)	Co$_1$Cr$_{66}$Zr$_{33}$
	LAVES (C15)	Co$_9$Cr$_{58}$Ti$_3$Nb$_{18}$Zr$_{12}$		BCC 2	Co$_{50}$Ti$_{23}$Zr$_{27}$
1000°C	LAVES (C15)	Co$_{12}$Cr$_{54}$Ti$_3$Nb$_8$Zr$_{23}$		CoTi$_2$	Co$_{33}$Ti$_{67}$
	BCC 1	Cr$_3$Ti$_{13}$Nb$_{81}$Zr$_3$		BCC 1	Ti$_1$Nb$_{99}$
	BCC 2	Co$_{49}$Ti$_{27}$Nb$_1$Zr$_{23}$		CoZr$_3$	Co$_{25}$Zr$_{75}$
700°C	BCC 2	Co$_{49}$Ti$_{30}$Zr$_{21}$	20°C	LAVES (C15)	Cr$_{67}$Zr$_{33}$
	LAVES (C15)	Co$_3$Cr$_{63}$Ti$_1$Nb$_1$Zr$_{32}$		BCC 2	Co$_{50}$Ti$_{23}$Zr$_{27}$
	BCC 1	Cr$_1$Ti$_{27}$Nb$_{66}$Zr$_6$		CoTi$_2$	Co$_{33}$Ti$_{67}$
600°C	BCC 2	Co$_{49}$Ti$_{27}$Zr$_{24}$		BCC 1	Nb
	LAVES (C15	Co$_2$Cr$_{64}$Ti$_1$Zr$_{33}$		CoZr$_3$	Co$_{25}$Zr$_{75}$
	BCC 1	Ti$_{16}$Nb$_{80}$Zr$_4$			
	CoTi$_2$	Co$_{33}$Ti$_{67}$			
	BCC 3	Co$_4$Cr$_1$Ti$_{55}$Nb$_{13}$Zr$_{27}$			

C (CoCr)$_{22}$(TiNbZr)$_{78}$
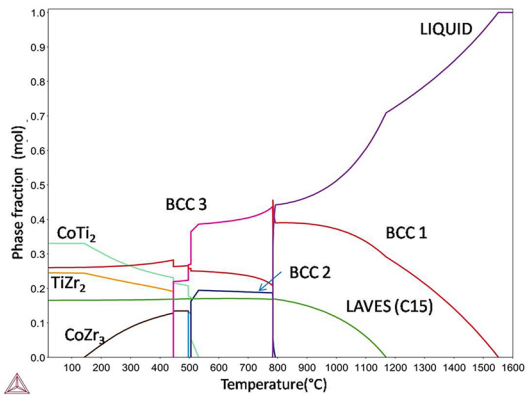
TEMPERATURE	PHASE	COMPOSITION	TEMPERATURE	PHASE	COMPOSITION
1300°C	LIQUID	Co$_{14}$Cr$_{12}$Ti$_{28}$Nb$_{16}$Zr$_{30}$	300°C	BCC 1	Ti$_2$Nb$_{97}$Zr$_1$
	BCC 1	Cr$_7$Ti$_{20}$Nb$_{62}$Zr$_{11}$		CoTi$_2$	Co$_{33}$Ti$_{67}$
1000°C	LIQUID	Co$_{20}$Cr$_5$Ti$_{33}$Nb$_7$Zr$_{35}$		TiZr$_2$	Ti$_{36}$Zr$_{64}$
	BCC 1	Cr$_4$Ti$_{25}$Nb$_{58}$Zr$_{13}$		Laves (C15)	Cr$_{66}$Zr$_{34}$
	LAVES (C15)	Co$_5$Cr$_{61}$Ti$_1$Nb$_4$Zr$_{29}$		CoZr$_3$	Co$_{25}$Zr$_{75}$
700°C	BCC 3	Co$_2$Cr$_1$Ti$_{43}$Nb$_{22}$Zr$_{32}$	20°C	BCC 1	Nb
	BCC 1	Ti$_{18}$Nb$_{73}$Zr$_9$		CoTi$_2$	Co$_{33}$Ti$_{67}$
	BCC 2	Co$_{50}$Ti$_{22}$Zr$_{28}$		TiZr$_2$	Ti$_{36}$Zr$_{64}$
	LAVES (C15)	Co$_4$Cr$_{62}$Ti$_1$Zr$_{33}$		Laves (C15)	Cr$_{67}$Zr$_{33}$
				CoZr$_3$	Co$_{25}$Zr$_{75}$

Fig. 5 Calculated phase diagrams for the synthetized alloys. (**A**) (CoCr)$_{52}$(TiNbZr)$_{48}$ alloy. (**B**) (CoCr)$_{40}$ (TiNbZr)$_{60}$ and (**C**) (CoCr)$_{22}$(TiNbZr)$_{78}$
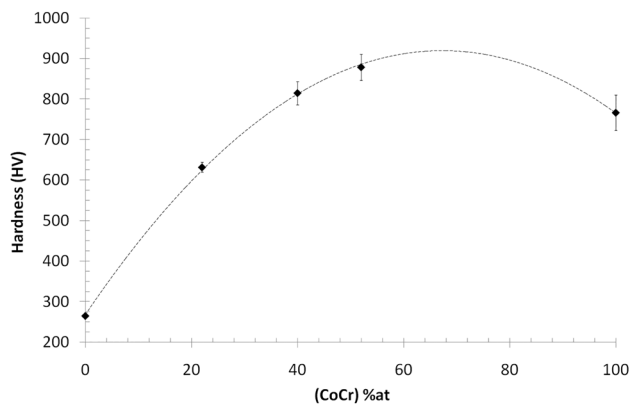
Fig. 6 Hardness test results for tested alloys as a function of CoCr concentration
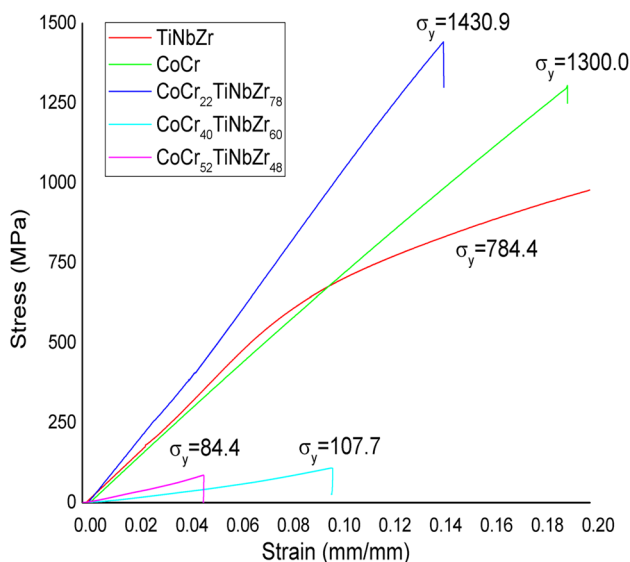

Fig. 7 Compression test results for tested alloys

the mechanical point of view, the hardness test results were strongly related to the intermetallic phase formation with the CoCr additions, showing a maximum of 876 HV for $X = 78$. Meanwhile, the yield strength was dominated by the amount of BCC 1.

References

1. S. Ranganathan, Alloyed pleasures: multimetallic cocktails. Curr. Sci. **85**, 1404–1406 (2003)
2. B. Cantor et al., Microstructural development in equiatomic multicomponent alloys. Mater. Sci. Eng. A. **375–377**, 213–218 (2004)
3. J.-W. Yeh et al., Nanostructured high-entropy alloys with multiple principal elements: novel alloy design concepts and outcomes. Adv. Eng. Mater. **6**, 299–303 (2004)
4. M.C. Gao et al., *High-entropy alloys* (Springer, Cham, 2016)
5. Q. Meng et al., A β-type TiNbZr alloy with low modulus and high strength for biomedical applications. Progr. Nat. Sci. Mater. Int. **24**, 157–162 (2014)
6. M. Niinomi, Metallic biomaterials. J. Artif. Organs. **11**, 105–110 (2008)
7. K. Prasad et al., Metallic biomaterials: current challenges and opportunities. Materials. **10**(8), 884 (2017)
8. M. Kaya et al., Microstructure characterization and biocompatibility behaviour of TiNbZr alloy fabricated by powder metallurgy. Mater. Res. Express. **6**, 126560 (2019)
9. T. Narushima, K. Ueda, Alfirano, Co-Cr alloys as effective metallic biomaterials, in *Advances in metallic biomaterials.* ed. by M. Niinomi, T. Narushima, M. Nakai (Springer, Berlin, 2015), pp.157–178
10. A. Shokrani, V. Dhokia, S.T. Newman, Cryogenic high speed machining of cobalt chromium alloy. Proc. CIRP. **46**, 404–407 (2016)
11. N. Maruyama et al., Friction-Wear Properties of Nickel-Free Co–Cr–Mo Alloyin a Simulated Body Fluid. Mater. Trans. **46**, 1588–1592 (2005)
12. D.B. Miracle, O.N. Senkov, A critical review of high entropy alloys and related concepts. Acta Mater. **122**, 448–511 (2017)
13. X. Yang, Y. Zhang, Prediction of high-entropy stabilized solid-solution in multi-component alloys. Mater. Chem. Phys. **132**(2), 233–238 (2012)
14. A.R. Miedema, F.R. Boer, R. Boom, Model predictions for the enthalpy of formation of transition metal alloys. Calphad. **1**, 341–359 (1977)
15. A.R. Miedema, P.F. Chatel, F.R. Boer, Cohesion in alloys-Fundamentals of a semi-empirical Model. Physica. **100B**, 1–28 (1980)
16. A.R. Miedema, Simple model for alloys. Philips Technol. Rev. **33**(6), 149–160 (1973)
17. Y. Zhang, X. Yang, P.K. Liaw, Alloy design and properties optimization of high-entropy alloys. JOM. **64**, 830–838 (2012)
18. Y. Zhang et al., Solid-solution phase formation rules for multi-component alloys. Adv. Eng. Mater. **10**, 534–538 (2008)
19. J.-W. Yeh, Physical metallurgy of high-entropy alloys. Miner. Metals Mater. Soc. **67**, 2254–2361 (2015)
20. S. Yang, G. Liu, Y. Zhong, Revisit the VEC criterion in high entropy alloys (HEAs) with high-. J. Alloys Compd. **916**, 165477 (2022)
21. S. Guo, C.T. Liu, Phase stability in high entropy alloys: Formation of. Progr. Nat. Sci. **21**, 433–446 (2011)

22. T. Zhang et al., Microstructure and mechanical properties of Cr doped WCoB based cermets by spark plasma sintering and first principle calculation. Progr. Nat. Sci. Mater. Int. **30**, 417–423 (2020)

23. S. Limmahakhum et al., Stiffness and strength tailoring of cobalt chromium graded cellular structures for stress-shielding reduction. Mater. Des. **114**, 633–641 (2017)

24. Y. Koizumi et al., Strain-induced martensitic transformation near twin boundaries in a biomedical Co–Cr–Mo alloy with negative stacking fault energy. Acta Mater. **61**, 1648–1661 (2013)

25. Z.-Y. He et al., Mechanical and corrosion properties of Ti-35Nb-7Zr-xHA composites fabricated by spark plasma sintering. Trans. Nonferrous Metals Soc. China. **27**, 848–856 (2017)

26. K.H. Lieser, H. Witte, Untersuchungen in den ternaeren Systemen Mg-Cu-Zn, Mg-Ni-Zn und Mg-Cu-Ni. Int. J. Mater. Res. **43**, 396–401 (1952)

27. V. Wagner, M. Conrad, B. Harbrecht, The m-phase of Co~6.3~Nb~6.7~. Acta Crystallogr. Sect. C. **51**(7), 1241–1243 (1995)

28. P.I. Kripyakevich, V.V. Burnashova, and V.Y. Markiy, The crystal structure of the compound Zr3Co. Dopovidi Akademii Nauk Ukrains'koi RSR, Seriya A: Fiziko-Tekhnichni taMatematichni Nauki, pp. 551-553 (1970).

29. F. Cruz-Gandarilla et al., XRD studies of Co-Fe-Ti nanocrystaline intermetallics. Mater. Sci. Forum. **444**, 109–114 (2003)

30. P.A. Farrar, S. Adler, On the system titanium-zirconium". Trans. Metall. Soc. Aime. **236**, 1061–1064 (1966)

31. Z.X. Guo, *The deformation* (Woodhead Publishing Limited, Cambridge, 2000)

32. K. He et al., Method for determining crystal grain size by X-ray diffraction. Cryst. Res. Technol. **53**(2), 1700157 (2018)

33. M. Hawryluk et al., Influence of the grade of hot work tool steels and its microstructural features on the durability of punches used in the closed die precision forging of valve forgings made of nickel-chrome steel. Wear. **204963**, 528–529 (2023)

34. J. Chen et al., A review on fundamental of high entropy alloys with promising high-temperature properties. J. Alloys Compd. **760**, 15–30 (2018)

35. X.-X. Yu, C.-Y. Wang, The effect of alloying elements on the dislocation climbing velocity in Ni: A first-principles study. Acta Mater. **57**, 5914–5923 (2009)

36. K. Zhao et al., Room temperature homogeneous flow in a bulk metallic glass with low glass transition temperature. Appl. Phys. Lett. **98**, 141313 (2011)

37. B. Cao et al., Precipitation-hardened high-entropy alloys for high-temperature applications: a critical review. MRS Bull. **44**, 854–859 (2019)

38. W.-R. Wang et al., Effects of Al addition on the microstructure and mechanical property of AlxCoCrFeNi high-entropy alloys. Intermetallics. **26**, 44–51 (2012)